physica status solidi rrl
www.pss-rapid.com

Evolution of Low-Frequency Vibrational Modes in Ultrathin GeSbTe Films

Eugenio Zallo, Daniele Dragoni, Yuliya Zaytseva, Stefano Cecchi, Nikolai I. Borgardt, Marco Bernasconi, and Raffaella Calarco*

GeSbTe (GST) phase-change alloys feature layered crystalline structures made of lamellae separated by van der Waals (vdW) gaps. This work sheds light on the dependence of interlamellae interactions at the vdW gap on film thickness of GST alloys as probed by vibrational spectroscopy. Molecular beam epitaxy is used for designing GST layers down to a single lamella. By combining density-functional theory and Raman spectroscopy, a direct and simple method is demonstrated to identify the thickness of the GST film. The shift of the vibrational modes is studied as a function of the layer size, and the low-frequency range opens up a new route to probe the number of lamellae for different GST compositions. Comparison between experimental and theoretical Raman spectra highlights the precision growth control obtained by the epitaxial technique.

Phase-change materials (PCMs), such as GeSbTe (GST) chalcogenide alloys on the GeTe–Sb_2Te_3 tie line, play a leading role as rewriteable optical storage media[1] and nonvolatile memories[2] due to their fast and reversible transition between the amorphous and the metastable crystalline phases. Despite longstanding efforts to identify alternative alloys with improved features, $Ge_2Sb_2Te_5$ (GST225) is still preferred for practical applications.[3] Amorphous GST225 crystallizes into a metastable cubic phase with stoichiometric vacancies on the cation sublattice, which turns into the trigonal ground state phase by further heating.[3] Insights into the properties of these two phases are still coveted due to their technological relevance.[4] The trigonal phase has a layered structure with lamellae, nine layers thick, separated by van der Waals (vdW) gaps. Several works have shown the importance of the ordering of vacancies in the cubic phase, which leads to the transformation into the trigonal phase with the formation of the vdW gaps[5,6] separating the lamellae. The transition from an Anderson insulator to a metal induced by vacancy ordering has also been deeply investigated.[7,8] On the contrary, less attention has been paid on the dependence of the material properties on the crystal thickness once this is reduced to few lamellae. In this respect, the study of the 2D character of the material by looking at the weak interlamellae interactions[9] is of particular interest.

Precise information on the size of thin-layer film can be obtained by high-resolution transmission electron microscopy (HRTEM),[10] but both sample preparation and statistical analysis make the estimate of film thickness laborious. This work demonstrates the control of the epitaxial GST225 down to a single lamella unveiling the unexplored low-frequency region of the Raman spectrum. By reducing the thickness of the film, the evolution of the peak positions with film thickness has been investigated. Calculations based on density-functional theory (DFT) allow for a clear identification of the experimental Raman peaks, confirming the trends observed experimentally. It turns out that the in-plane E_g and out-of-plane A_{1g} modes between 30 and 40 cm^{-1} can probe the weak interaction at the vdW gap resulting in a direct measure of the film thickness. Thermal annealing of the GST225 series leads to the formation of Ge-poor compositions with similar dependencies of the Raman peaks on the film thickness.

The layered GST films were grown by solid-source molecular beam epitaxy (MBE) on Si(111) surfaces. The quasi-vdW epitaxy has been obtained by Sb passivation of the Si surfaces to eliminate surface dangling bonds (see Experimental Section).[11] **Figure 1**a shows the ω–2ϑ scans from X-ray diffraction (XRD) of the GST series by reducing the thickness from 34.3 to

Dr. E. Zallo,[+] Dr. S. Cecchi, Dr. R. Calarco
Paul-Drude-Institut für Festkörperelektronik
Leibniz-Institut im Forschungsverbund Berlin e.V.
Hausvogteiplatz 5-7, D-10117 Berlin, Germany
E-mail: eugenio.zallo@wsi.tum.de

Dr. D. Dragoni, Prof. M. Bernasconi
Department of Materials Science
University of Milano-Bicocca
via R. Cozzi 55, 20125 Milano, Italy

Y. Zaytseva, Prof. N. I. Borgardt
Electron Microscopy Lab.
National Research University of Electronic Technology (MIET)
Zelenograd 124498, Moscow, Russia

Dr. R. Calarco
CNR Institute for Microelectronics and Microsystems–IMM
Consiglio Nazionale delle Ricerche
Via del Fosso del Cavaliere 100, 00133 Roma, Italy

The ORCID identification number(s) for the author(s) of this article can be found under https://doi.org/10.1002/pssr.202000434.

[+]Present address: Walter-Schottky-Institut and Physik Department, Technische Universität München, Am Coulombwall 4, 85748 Garching, Germany

© 2020 The Authors. Physica Status Solidi (RRL) – Rapid Research Letters published by Wiley-VCH GmbH. This is an open access article under the terms of the Creative Commons Attribution License, which permits use, distribution and reproduction in any medium, provided the original work is properly cited.

DOI: 10.1002/pssr.202000434

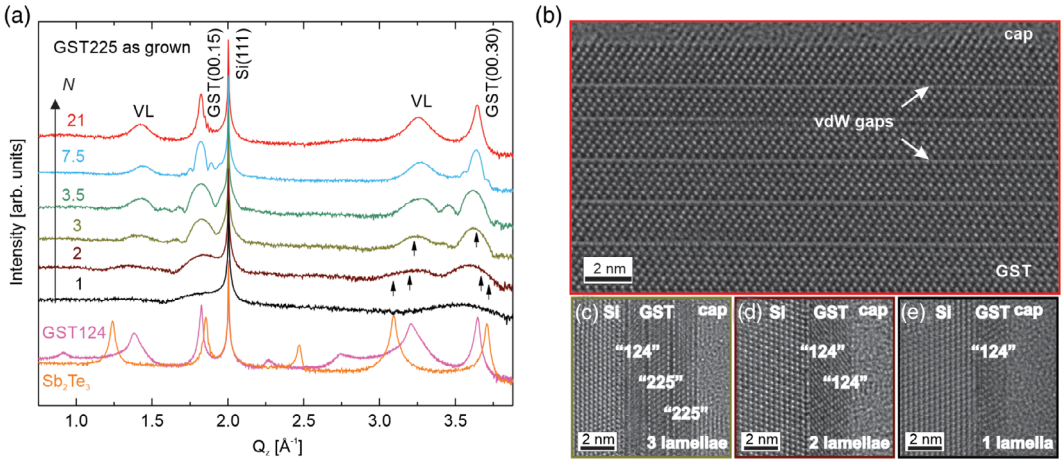

Figure 1. Engineered nanometer scale GST225 chalcogenide. a) XRD ω–2ϑ scans for layered crystalline GST grown on Si(111) with number of lamellae $N \approx 21$, 7.5, 3.5, 3, 2, and 1. The orange and pink curves are the as-grown Sb_2Te_3 and GST124 samples, respectively. b) HRTEM image of the specimen in Si[1$\bar{1}$0] zone axis with $N \approx 21$. VdW gaps occur mainly every nine atomic layers. c–e) HRTEM images for films with three lamellae (c), two lamellae (d), and one lamella (e), showing the examples of Ge-poor GST blocks at the interface with the substrate due to the transient growing condition discussed in the text.

2.3 nm (estimated by X-ray reflectivity (XRR) measurements; see Table S1, Supporting Information). The symmetric scan of the bulk-like sample (top red curve) confirms that the layer is oriented along (111) with Bragg reflection of the Si substrate at $Q_z = 2.00\,\text{Å}^{-1}$ and the (00.15) and (00.30) reflections of GST225 at $Q_z = 1.83$ and $3.67\,\text{Å}^{-1}$, respectively.[12] The reflections (00.12) and (00.27) at $Q_z = 1.38$ and $3.22\,\text{Å}^{-1}$, respectively, have been assigned in our previous work[8] to the first-order peaks of the vacancy layers (VLs) and prove the layered nature of the film even though the larger full width at half maximum (FWHM) is an indication of compositional disorder[8] (see Figure S1, Supporting Information). In addition, they allow for the estimate of the average block size of 16.2 Å, which means a total number of lamellae (N) of $\approx$21 in the bulk-like sample (the number of lamellae reported in the text has been obtained by the thickness/block size ratio; see Table S1, Supporting Information, and the values have been approximated either to full- or half-filled lamella for the sake of clarity). Furthermore, the HRTEM analysis of this sample (Figure 1b) highlights the areas with mainly nine-layer blocks (GST225) separated by vdW gaps and a lattice stacking compatible with the trigonal phase.[13] The determination of the stacking has been possible only in local areas of the TEM specimens due to a clear contrast between vdW gaps and atoms (see Figure S2, Supporting Information). The discrepancies in other regions are attributed to slight deviation from the high symmetry orientation or to the presence of bilayer (BL) defects.[14]

The dependence of the structural properties on the thickness of the film has been investigated by XRD. The diffraction pattern of seven samples with different thickness, reported in Figure 1a, shows two main changes with the thickness of the film; namely, the FWHM of the GST(00.30) reflections increases from $0.03\,\text{Å}^{-1}$ ($N \approx 21$) to $0.22\,\text{Å}^{-1}$ ($N \approx 2$), and the VL peak intensity decreases by reducing the number of vdW gaps. HRTEM images correlate with XRD data and demonstrate the successful realization of GST films down to 3, 2, and 1 lamellae, as shown, respectively, in Figure 1c–e. However, TEM studies establish that the crystal structure becomes more perfect with a regular arrangement of vdW gaps with increasing GST film thickness. It should also be pointed out that the 1–2 lamellae GST films could vary somewhat in the thickness and contain amorphous regions. Albeit the average composition corresponds to GST225 throughout the series and no significant change of the in-plane lattice constant is detected down to $N \approx 3.5$ (1.6941 Å vs 1.6935 Å for bulk-like; see Figure S3, Supporting Information), HRTEM evidences a local tendency to form Ge-poor configurations such as GST124 and Sb_2Te_3 close to the Si substrate, which is also confirmed by the results of energy-dispersive X-ray (EDX) microanalysis on the average stoichiometry of the GST films (see Table S2, Supporting Information). This can be ascribed to kinetic effects during the shutter transient at the beginning of the growth, and examples are reported in Figure 1c–e for $N \approx 3$–1, respectively. In particular, the XRD spectrum for two lamellae shows the smearing out of the VL peak (see arrows in Figure 1a).

Raman spectra of the layered GST225 as a function of layer thickness are reported in **Figure 2**a. From DFT calculations and polarization resolved measurement at 10 K, the symmetry of the vibrational modes is assigned. Bulk phonons at the Γ-point actually correspond to the irreducible representations $\Gamma = 4E_g \oplus 4A_{1g} \oplus 4E_u \oplus 4A_{2u} \oplus E_u^T \oplus A_{2u}^T$. High-frequency modes can be identified in the bulk-like sample, such as E_g (3), A_{1g} (2), and A_{1g} (4) at 107.4, 110.7, and $175.1\,\text{cm}^{-1}$, respectively (the peak positions have been obtained by the low-temperature measurements at 10 K of Figure S5, Supporting Information). Interestingly, two other modes are visible in the low-frequency region: E_g (1) at $36.7\,\text{cm}^{-1}$ and A_{1g} (1) at $53.7\,\text{cm}^{-1}$. Although these modes have been already observed in a previous work,[15] in the following, we will show that their dependence on the sample thickness allows estimating the number of lamellae, which represents the main result of this work.

Overall, Figure 2b shows a good agreement between experiment and theory for the intensity and position of

© 2020 The Authors. Physica Status Solidi (RRL) – Rapid Research Letters published by Wiley-VCH GmbH

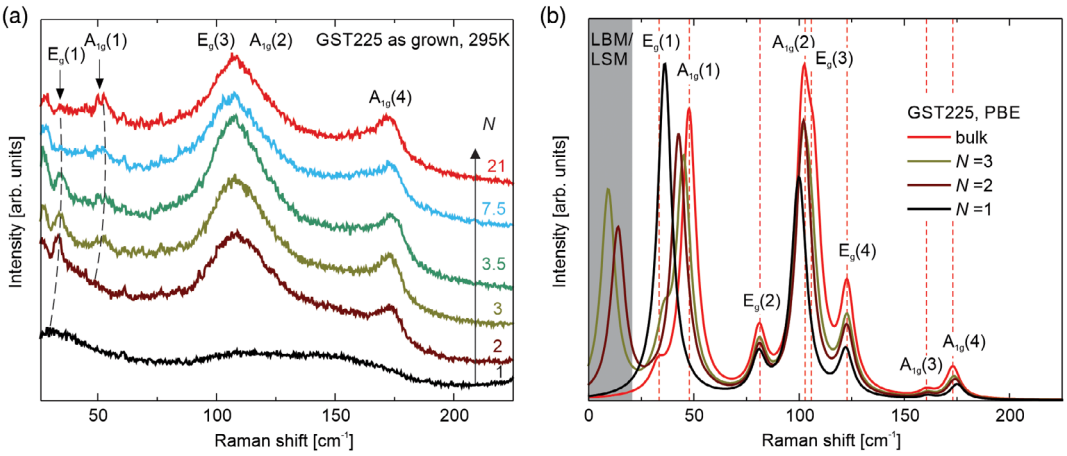

Figure 2. Raman spectra and intensity of GST225 as a function of number of layers. a) Stokes Raman spectra at RT of GST grown on Si(111) with $N \approx 21$ (red), 7.5 (light blue), 3.5 (green), 3 (olive), 2 (brown), and 1 (black). The narrow peak at 49.7 cm^{-1} on the lower energy side of the A_{1g} (1) mode is attributed to coherent anti-Stokes Raman scattering of air.[38] b) Raman intensity of GST225 in bulk and thin-film geometries calculated with DFT phonons and the bond polarizability model (BPM) in the $z(y,xy)$–z scattering geometry. Modes at ultralow frequencies (LBM/LSM) become active as long as translational symmetry is broken along the c-axis and at least two lamellae are present.

Raman peaks. The inversion of the relative position of the theoretical E_g (3) and A_{1g} (2) modes (predicted only 8.3 cm^{-1} apart) with respect to the experiment (see Figure S4, Supporting Information) can be attributed to the lack of both disorder within the cationic sublattice and compositional disorder[16] in the theoretical models. The E_g (2), A_{1g} (3), and E_g (4) modes present in the theoretical Raman spectra are hidden in the experimental spectra at room temperature (RT) due to low signal-to-noise ratio. Raman spectra at low temperature, however, allow for resolving a shoulder on the lower energy side of the A_{1g} (4) peak, which can be attributed to the A_{1g} (3) mode (see Figure S5, Supporting Information).

Figure 2a evidences two different trends for low- and high-frequency Raman peaks as a function of thickness down to two lamellae. The weak signal for $N \approx 1$ is due to the reduced amount of material, and the smearing out of the peaks resembles the spectrum of the disordered cubic phase reported in the previous study.[17] In addition, XRD and HRTEM data (see Figure 1) show only the GST diffraction peaks and no clear vdW gap. Albeit the high-frequency modes (E_g (3), A_{1g} (2), and A_{1g} (4)) are almost not affected by the film thickness (see also Figure S4, Supporting Information), the low-frequency modes (E_g (1) and A_{1g} (1)) nicely show a clear shift. We define now the nomenclature E_g^B (1) and A_{1g}^B (1) for the low-frequency modes in thin layers that evolve into the E_g (1) and A_{1g} (1) bulk modes by increasing the thickness. The frequency evolution reported in **Figure 3** for the measurement at 10 K (full symbols) shows that both E_g^B (1) and A_{1g}^B (1) soften by reducing the thickness (for the $1/N$ values, see Table S1, Supporting Information). The total shift for E_g^B (1) is $\approx$2 cm^{-1} between $N \approx 21$ (bulk-like) and $N \approx 2$, whereas the decrease in intensity of A_{1g}^B (1) makes the tracing of the peak possible only down to three lamellae (see Figure 2a) with a total shift of $\approx$1 cm^{-1}. The theoretical calculations performed for bulk and $N = 3$, 2, and 1 (the phonon modes data for GST225 are reported in the Supporting Information) confirm the experimental redshift between bulk and $N = 2$ for E_g^B (1) of 2.5 cm^{-1} and a slightly larger value between bulk and $N = 3$ for A_{1g}^B (1) of 2.6 cm^{-1}. At the same time, the maximum theoretical shift (between bulk and $N = 1$) for E_g^B (1) and A_{1g}^B (1) is $\approx$3.5 and $\approx$11.6 cm^{-1}, respectively. The not perfect matching of the A_{1g}^B (1) for $N \approx 3$ with theory can be explained by the compositional disorder due to the Ge depletion occurring in some areas of the film (see Figure 1c) that can affect the vibrational frequencies.

Useful insights into the frequency change of the E_g^B (1) and A_{1g}^B (1) modes can be found by looking at their displacement patterns (Figure 3b). The low-frequency modes consist, respectively, of in-plane and out-of-plane vibrations where the two edges of the lamella move in opposite direction and modulate more the weaker interactions between the lamellae (interlamellar) than the stronger ones within the lamella (intralamellar). The different behavior of the high-frequency modes with thickness is attributed to the antiphase vibrations of the atoms near the edge of the lamella (see Figure S4, Supporting Information), which reduce the overall effect. Interestingly, the sensitivity to the vdW gap of the E_g (1) and A_{1g} (1) allows for probing the layer thickness, and analogies can be found, respectively, with the interlayer shear (LSM) and breathing (LBM) modes in 2D materials, such as MoS_2,[18] Bi_2Te_3,[19] graphene,[9] and vdW heterostructures.[20] In fact, LSMs and LBMs are also present in bulk GST225, but at variance with MoS_2, they are Raman-silent, being zone-boundary modes in the primitive trigonal cell. Nonetheless, the breaking of the lattice translational symmetry due to finite thickness along the c-axis activates these modes in the Raman spectrum at E_g^B (1) = 7.1 (10) cm^{-1} and A_{1g}^B (1) = 9.3 (13.9) cm^{-1} for the $N = 3$ (2) case, respectively (see the gray area of Figure 2b). Unfortunately, this frequency region is very close to the Rayleigh peak, and it is not experimentally accessible by our setup. In the rest of the manuscript, we will then focus on the low-frequency modes in the region 30–40 cm^{-1} as a probe for the number of lamellae in GST materials with different compositions.

To strengthen the observation of the thickness dependence of the low-frequency Raman modes in GST materials due to their

© 2020 The Authors. Physica Status Solidi (RRL) – Rapid Research Letters published by Wiley-VCH GmbH

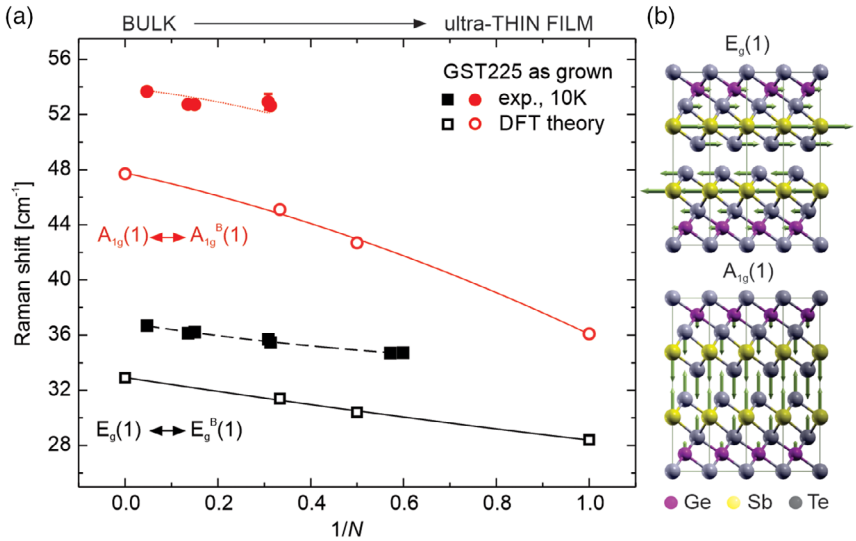

Figure 3. Raman shift of low-frequency modes of as-grown GST225 as a function of inverse number of layers. a) Peak positions for E_g^B (1) mode (filled black squares) and A_{1g}^B (1) (filled red circles) that evolve into the E_g (1) and A_{1g} (1) bulk modes, respectively, as a function of inverse number of lamellae (see Table S1, Supporting Information, for the full dataset). The corresponding theoretical DFT frequencies at 0 K are shown by open symbols. The continuous and dashed lines are polynomial fits. The dotted line is a guide to the eye. b) Displacement patterns for the E_g (1) and A_{1g} (1) modes in the bulk.

interlamellar character, the analysis reported for GST225 has been repeated for a different composition of the alloy that was obtained by rapid thermal annealing (RTA) of the GST225 series at 300 °C for 30 min in N_2 atmosphere. This results for the bulk-like sample in the formation of GST124,[21,22] which has a lower formation energy than GST225,[13] as confirmed by the average block size of 1.4 Å ($N \approx 23.5$; see Figure S6, Supporting Information).

The irreducible representation of phonons at the Γ-point for GST124 bulk is $\Gamma = 3E_g \oplus 3A_{1g} \oplus 3E_u \oplus 3A_{2u} \oplus E_u^T \oplus A_{2u}^T$, and five active modes are visible in the spectrum at RT of **Figure 4**a (red curve), namely, E_g (1) and A_{1g} (2) at 36.5 and 55.6 cm^{-1} (low frequency), respectively, and A_{1g} (2), E_g (3), and A_{1g} (3) at 106.7, 112.5, and 173.5 cm^{-1} (high frequency), respectively. The peak positions for A_{1g} (2) and E_g (3) were obtained from polarization resolved Raman spectra, whereas a low signal-to-noise ratio makes the assignment for E_g (2) difficult. Similar to the GST225 case, there is an inversion of the theoretical A_{1g} (2) with E_g (3) peak positions as compared with experimental data. The Raman spectrum for bulk GST124 reported in Figure 4a matches

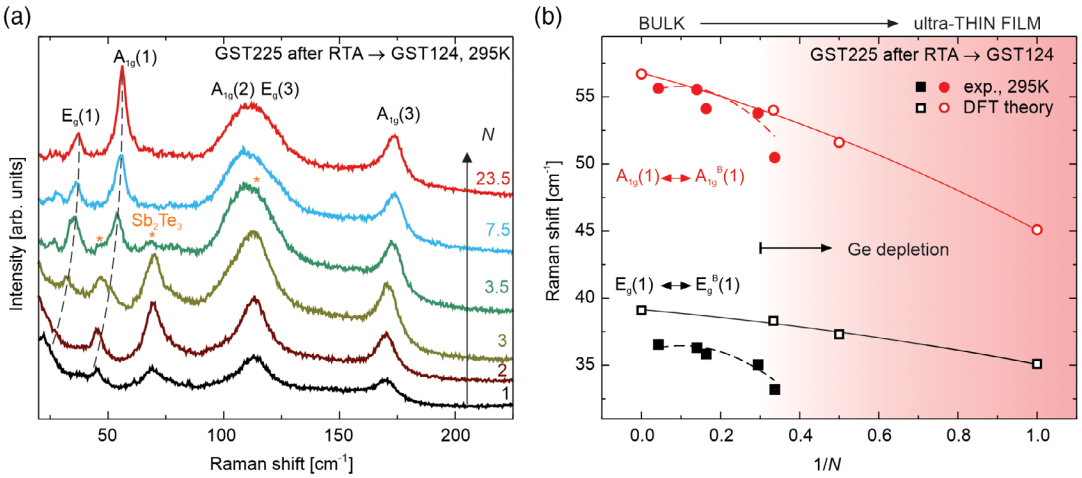

Figure 4. Raman spectra of GST225 after RTA as a function of number of layers. a) Stokes Raman spectra at RT after RTA of GST grown on Si(111) with $N \approx 23.5$ (red), 7.5 (light blue), 3.5 (green), 3 (olive), 2 (brown), and 1 (black) lamellae. b) Peak positions for the E_g^B (1) mode (filled black squares) and A_{1g}^B (1) (filled red circles) that evolve into the E_g (1) and A_{1g} (1) bulk modes, respectively, as a function of inverse number of lamellae (see Table S1, Supporting Information, for the full dataset). The corresponding theoretical DFT frequencies at 0 K are shown by open symbols. The continuous and dashed lines are polynomial fits.

© 2020 The Authors. Physica Status Solidi (RRL) – Rapid Research Letters published by Wiley-VCH GmbH

well with the DFT calculations (see Figure S7, Supporting Information). Most importantly, the overall spectrum is characterized by sharper peaks, especially in the low-frequency region. For example, the FWHM for A_{1g} (1) in the bulk-like sample measured at 10 K decreases from 5.9 cm^{-1} (as-grown GST225) to 4 cm^{-1} (annealed GST225). This is due to the improved ordering of the VLs[12,14] resulting in the reduction of chemical disorder.[23] Down to $N \approx 7$, the low-frequency modes redshift, whereas the high-frequency modes do not show a significant change (see Figure 4, and Figure S8, Supporting Information, and the $1/N$ values are reported in Table S1, Supporting Information). In the case of GST124 as well, the E_g (1) and A_{1g} (1) vibrations mostly modulate the interaction across the vdW gap than those inside the lamella. Besides the similarities with the as-grown case, new features appear for $N \approx 3.5$ at 46.3, 69.5, and 113 cm^{-1}. These peaks correspond to the E_g (1), A_{1g} (1), and E_g (2) Raman modes of bulk Sb_2Te_3, respectively.[24] The tendency to form Sb_2Te_3 at the beginning of the growth was already observed for as-grown GST225 (see Figure 1, $N \approx 2$), but no clear features were measured in the Raman spectrum, probably due to the reduced amount of material. In the annealed case, by decreasing the thickness down to $N \approx 1$, the Sb_2Te_3 features become even more pronounced in the overall spectrum with the redshift of the high-frequency mode to 169.7 cm^{-1} at $N \approx 3$, corresponding to the A_{1g} (2) mode in Sb_2Te_3. This phase separation might be ascribed to a decrease of the energy gain of GST with respect to Sb_2Te_3 and GeTe by reducing the film thickness.[25] In our case, annealing might lead to material segregation, such as Ge or formation of GeTe BLs, whose evaporation is prevented by the capping layer. Contrary to Sb BLs, whose Raman features are easily detected in epitaxial $Sb_{2+x}Te_3$ films,[26] a poor GeTe signal for ultrathin films below four BLs has been shown by Wang et al.[27] to be driven by the suppression of Peierls distortions in the thinner samples. Recently, Lotnyk et al. observed Ge evaporation during deposition of GST225 at higher temperature with the formation of GST124, $GeTe_2$, and Sb_2Te_3,[28] but no additional modes are visible in our spectrum that could be attributed to $GeTe_2$. Further studies are needed to shed light on the stacking in the annealed samples in the presence of capping.

Even though Sb_2Te_3 dominates the full spectrum, it is still possible to follow the low-frequency GST modes between $N \approx 23.5$ (bulk-like) and $N \approx 3$: softening of the modes with decreasing thickness is observed with a total shift for E_g^B (1) and A_{1g}^B (1) of ≈3.3 and 5.2 cm^{-1}, respectively (see Figure 4b, and the $1/N$ values are reported in Table S1, Supporting Information). The polarization resolved Raman spectra of the sample with $N \approx 3$ allowed for discriminating the E_g (1) of Sb_2Te_3 from the A_{1g}^B (1) of GST124. An increased Rayleigh scattering due to a larger surface roughness prevented instead a good fit of the E_g^B (1) peak at $N \approx 2$. The peak positions from the theoretical calculations of GST124 in bulk and in thin layers with $N = 1$, 2, and 3 (see Supporting Information for the data) evidence softening with a total shift between bulk and $N = 1$ for E_g^B (1) and A_{1g}^B (1) of ≈4 and ≈11.6 cm^{-1}, respectively. The comparison of the fits for the experimental and theoretical data shows a good agreement down to $N = 3.5$, where the Sb_2Te_3 signature becomes visible. The larger softening of the experimental frequencies between $N = 3.5$ and $N = 3$ is qualitatively ascribed to the Ge deficiency resulting in the increase of the atomic distances between blocks and the decrease of the restoring forces. It is important to note that LBM and LSM are Raman-silent also in bulk GST124, because they correspond to zone-boundary modes in the primitive cell, but they become Raman active for $N = 3$ (E_g (1) = 8.9 cm^{-1}, A_{1g} (1) = 11.4 cm^{-1}) and $N = 2$ (E_g (1) = 12.2 cm^{-1}, A_{1g} (1) = 16.5 cm^{-1}), as a result of the breaking of translational symmetry along the c-axis (see Figure S7, Supporting Information).

In conclusion, we have investigated the dependence on the sample thickness of the vibrational properties of ultrathin GST films epitaxially grown by MBE. A method for probing the number of lamellae in layered GST materials has been proposed by means of Raman spectroscopy, a tool for nondestructive characterization that has been already used for PCM materials.[12,8,29,30] Indeed, we have demonstrated that the number of lamellae can be measured by following the change of low-frequency Raman modes with the film thickness down to a single lamella. This has been shown for GST225 and for GST124 obtained, in turn, by post-growth annealing of a GST225 series. The methodology is quick and robust and highlights the advantages of the MBE technique for the precise control of the layer size.

Experimental Section

MBE Growth: The studied samples consist of GST films with the thicknesses between 34.3 and 2.3 nm grown by solid-source MBE on Si(111)–($\sqrt{3} \times \sqrt{3}$)R30°–Sb passivated surfaces with 0.03° miscut. All the substrates are cleaned, and the surfaces are prepared using the methods described in previous works.[11,31] According to flux calibration by XRR measurements on amorphous Ge, Sb, and Te films grown at RT, the cell temperatures correspond to a Ge/Sb/Te flux ratio of ≈2/2/5. The substrate temperature was ≈250 °C for all the growths. A reflection high-energy electron diffraction (RHEED) technique was used for confirming the formation of the Si(111) − (7 × 7) reconstruction prior the Sb termination of the substrate.

XRD and XRR: Ex situ structural characterization of the films was performed by high-resolution XRD and XRR. The system consists of a four-circle PANalytical X'Pert Pro Materials Research diffractometer equipped with a Ge (220) hybrid monochromator and Cu Kα_1 (λ = 1.540598 Å) X-ray radiation. For ω–2ϑ scans, a 1 mm slit at the detector side was used. The cubic unit cell has been adopted for indexing the XRD pattern of the Si substrate, whereas the choice of the trigonal unit cell in the case of the epilayer accounts for the study of the rhombohedral layered GST structure with space group R-3m.

DFT: Phonons are calculated at Γ-point within density-functional perturbation theory (DFPT)[32] as implemented in the Quantum-Espresso suite.[33] We used the Perdew–Burke–Ernzerhof (PBE) exchange and correlation functional[34] and the semiempirical correction due to Grimme (D2)[35] to include vdW interactions. We used norm conserving pseudopotentials and a plane wave expansion of Kohn–Sham orbitals up to an energy cutoff of 30 Ry. Brillouin zone integration is performed on Monkhorst–Pack[36] grids with a minimal k-point linear density of 4.6 Å. Bulk GST124 and GST225 are modeled in the fully relaxed primitive cells with 3D periodic boundary conditions. Thin films are instead modeled by trigonal cells at the theoretical bulk in-plane lattice parameter (a = 4.191 Å for GST225 and a = 4.290 Å for GST124), containing $N = 1$, 2, and 3, seven-layer (GST124) or nine-layer (GST225) blocks plus a vacuum 12 Å wide separating the periodic images of the layers along the c-axis. The cationic layers close to the vdW gaps are fully occupied by Sb atoms,[37] and intermixing in the cationic sublattices is neglected in the present work. The theoretical Raman spectra are computed from ab initio phonons, and Raman tensors in nonresonant conditions are obtained, in turn, from the BPM developed previously for GST225.[30] A $z(x,xy)$–z

© 2020 The Authors. Physica Status Solidi (RRL) – Rapid Research Letters published by Wiley-VCH GmbH

backscattering geometry is considered with z along the c-axis of the trigonal representation of all models. A Lorentzian broadening of 3 cm^{-1} is assigned to all peaks. The Bose factor is computed at 300 K. The theoretical atomic positions and the size of the vdW gaps in bulk and multilayers of GST225 and GST124 are given in Table S3–S6 and Table S11–S14, Supporting Information. Theoretical phonons at the Γ-point in bulk and multilayers of GST225 and GST124 are given in Table S7–S10 and Table S15–S18, Supporting Information.

HRTEM: HRTEM studies were carried out in an FEI Titan Themis 80-200 transmission electron microscope operated at 200 kV and equipped with spherical aberration image corrector, FEI Ceta 16M complementary metal–oxide–semiconductor (CMOS) camera, and Super-X EDX detector. Cross-sectional TEM specimens in Si[1$\bar{1}$0] zone axis were prepared by a focused ion beam technique in a dual-beam workstation Helios NanoLab 650.

Micro-Raman Spectroscopy: The Stokes scattering of the samples was obtained by means of micro-Raman spectroscopy. The systems were excited by a continuous wave He–Ne laser 632.8 nm equipped with an LN_2-cooled charge-coupled device (CCD) detector in backscattering $z(y,xy)-z$ geometry. The emission was focused by a microscope objective with 0.9 (0.55) numerical aperture at 295 K (10 K), the power densities of 10^4 W cm^{-2} (25 kW cm^{-2}), and an acquisition time of 180 s. The same objective was used for the collection of the signal. The achieved spectral resolution is 0.7 cm^{-1}, and a notch filter suppressed the stray light. The character of the vibrational modes was assigned by means of polarization-resolved spectroscopy.

Supporting Information

Supporting Information is available from the Wiley Online Library or from the author.

Acknowledgements

The authors would like to thank M. Ramsteiner for fruitful discussions, and C. Stemmler and C. Hermann for their dedicated maintenance of the MBE system. Furthermore, the authors appreciate the critical reading of the manuscript by J. Herranz Zamorano. This work was partly funded by the Leibniz Gemeinschaft within the Leibniz Competition on a project entitled: "Epitaxial phase change superlattices designed for investigation of non-thermal switching," the European Union's Horizon 2020 research and innovation program under Grant Agreement No. 824957 ("BeforeHand:" Boosting Performance of Phase Change Devices by Hetero- and Nanostructure Material Design) and the Ministry of Science and Higher Education of the Russian Federation (State assignment No. FSMR-2020-0018). Open access funding enabled and organized by Projekt DEAL.

Conflict of Interest

The authors declare no conflict of interest.

Author Contributions

E.Z. designed the experiment. E.Z. performed the growths, carried out XRD and reflectivity, and thermal annealing, and analyzed the data. S.C. performed and analyzed the XRD reciprocal space maps. Y.Z. and N.I.B. carried out HRTEM and EDX investigations. E.Z. performed the Raman spectroscopy. The DFT, DFPT, and Raman spectra calculations were carried out by D.D. The analysis of Raman spectroscopy data and comparison with calculations was carried out by E.Z., D.D., and M.B. The article was written by E.Z. with the help and through contributions from all co-authors. E.Z. conceived the project. R.C. coordinated the project. All authors have given approval to the final version of the manuscript.

Keywords

2D materials, first principles, molecular beam epitaxy, phase-change materials, Raman

Received: September 10, 2020
Revised: October 10, 2020
Published online: November 19, 2020

[1] M. Wuttig, N. Yamada, *Nat. Mater.* **2007**, *6*, 824.
[2] G. W. Burr, M. J. Breitwisch, M. Franceschini, D. Garetto, K. Gopalakrishnan, B. Jackson, B. Kurdi, C. Lam, L. A. Lastras, A. Padilla, B. Rajendran, S. Raoux, R. S. Shenoy, *J. Vac. Sci. Technol. B Microelectron. Nanometer Struct.* **2010**, *28*, 223.
[3] I. Friedrich, V. Weidenhof, W. Njoroge, P. Franz, M. Wuttig, *J. Appl. Phys.* **2000**, *87*, 4130.
[4] S. W. Fong, C. M. Neumann, H. P. Wong, *IEEE Trans. Electron Devices* **2017**, *64*, 4374.
[5] J. Momand, R. Wang, J. E. Boschker, M. A. Verheijen, R. Calarco, B. J. Kooi, *Nanoscale* **2017**, *9*, 8774.
[6] A. Lotnyk, U. Ross, T. Dankwort, I. Hilmi, L. Kienle, B. Rauschenbach, *Acta Mater.* **2017**, *141*, 92.
[7] W. Zhang, A. Thiess, P. Zalden, R. Zeller, P. H. Dederichs, J.-Y. Raty, M. Wuttig, S. Blügel, R. Mazzarello, *Nat. Mater.* **2012**, *11*, 952.
[8] V. Bragaglia, F. Arciprete, W. Zhang, A. M. Mio, E. Zallo, K. Perumal, A. Giussani, S. Cecchi, J. E. Boschker, H. Riechert, S. Privitera, E. Rimini, R. Mazzarello, R. Calarco, *Sci. Rep.* **2016**, *6*, 23843.
[9] P. H. Tan, W. P. Han, W. J. Zhao, Z. H. Wu, K. Chang, H. Wang, Y. F. Wang, N. Bonini, N. Marzari, G. Savini, A. Lombardo, A. C. Ferrari, *Nat. Mater.* **2011**, *11*, 294.
[10] A. M. Mio, S. M. S. Privitera, V. Bragaglia, F. Arciprete, C. Bongiorno, R. Calarco, E. Rimini, *Nanotechnology* **2017**, *28*, 065706.
[11] J. E. Boschker, J. Momand, V. Bragaglia, R. Wang, K. Perumal, A. Giussani, B. J. Kooi, H. Riechert, R. Calarco, *Nano Lett.* **2014**, *14*, 3534.
[12] E. Zallo, S. Cecchi, J. E. Boschker, A. M. Mio, F. Arciprete, S. Privitera, R. Calarco, *Sci. Rep.* **2017**, *7*, 1466.
[13] J. Da Silva, A. Walsh, H. Lee, *Phys. Rev. B* **2008**, *78*, 224111.
[14] A. Lotnyk, T. Dankwort, I. Hilmi, L. Kienle, B. Rauschenbach, *Nanoscale* **2019**, *11*, 10838.
[15] E. Zallo, R. Wang, V. Bragaglia, R. Calarco, *Appl. Phys. Lett.* **2016**, *108*, 221904.
[16] N. Yamada, T. Matsunaga, *J. Appl. Phys.* **2000**, *88*, 7020.
[17] V. Bragaglia, K. Holldack, J. E. Boschker, F. Arciprete, E. Zallo, T. Flissikowski, R. Calarco, *Sci. Rep.* **2016**, *6*, 28560.
[18] X. Zhang, W. P. Han, J. B. Wu, S. Milana, Y. Lu, Q. Q. Li, A. C. Ferrari, P. H. Tan, *Phys. Rev. B: Condens. Matter Mater. Phys.* **2013**, *87*, 115413.
[19] Y. Zhao, X. Luo, J. Zhang, J. Wu, X. Bai, M. Wang, J. Jia, H. Peng, *Phys. Rev. B* **2014**, *90*, 245428.
[20] C. H. Lui, Z. Ye, C. Ji, K.-C. Chiu, C.-T. Chou, T. I. Andersen, C. Means-Shively, H. Anderson, J.-M. Wu, T. Kidd, Y.-H. Lee, R. He, *Phys. Rev. B* **2015**, *91*, 165403.
[21] V. Bragaglia, B. Jenichen, A. Giussani, K. Perumal, H. Riechert, R. Calarco, *J. Appl. Phys.* **2014**, *116*, 054913.
[22] J. Momand, R. Wang, J. E. Boschker, M. A. Verheijen, R. Calarco, B. J. Kooi, *Nanoscale* **2015**, *7*, 19136.
[23] H. Hardtdegen, S. Rieß, M. Schuck, K. Keller, P. Jost, H. Du, M. Bornhöfft, A. Schwedt, G. Mussler, M. van der Ahe, J. Mayer, G. Roth, D. Grützmacher, M. Mikulics, *J. Alloys Compd.* **2016**, *679*, 285.

© 2020 The Authors. Physica Status Solidi (RRL) – Rapid Research Letters published by Wiley-VCH GmbH

[24] G. C. Sosso, S. Caravati, M. Bernasconi, *J. Phys. Condens. Matter Inst. Phys. J.* **2009**, *21*, 095410.
[25] Y. Zheng, M. Xia, Y. Cheng, F. Rao, K. Ding, W. Liu, Y. Jia, Z. Song, S. Feng, *Nano Res.* **2016**, *9*, 3453.
[26] S. Cecchi, D. Dragoni, D. Kriegner, E. Tisbi, E. Zallo, F. Arciprete, V. Holý, M. Bernasconi, R. Calarco, *Adv. Funct. Mater.* **2019**, *29*, 1805184.
[27] R. Wang, D. Campi, M. Bernasconi, J. Momand, B. J. Kooi, M. A. Verheijen, M. Wuttig, R. Calarco, *Sci. Rep.* **2016**, *6*, 32895.
[28] A. Lotnyk, M. Behrens, B. Rauschenbach, *Nanoscale Adv.* **2019**, *1*, 3836.
[29] P. Němec, A. Moreac, V. Nazabal, M. Pavlišta, J. Přikryl, M. Frumar, *J. Appl. Phys.* **2009**, *106*, 103509.
[30] G. C. Sosso, S. Caravati, R. Mazzarello, M. Bernasconi, *Phys. Rev. B* **2011**, *83*, 134201.
[31] R. Wang, J. E. Boschker, E. Bruyer, D. D. Sante, S. Picozzi, K. Perumal, A. Giussani, H. Riechert, R. Calarco, *J. Phys. Chem. C* **2014**, *118*, 29724.
[32] S. Baroni, S. de Gironcoli, A. Dal Corso, P. Giannozzi, *Rev. Mod. Phys.* **2001**, *73*, 515.
[33] P. Giannozzi, S. Baroni, N. Bonini, M. Calandra, R. Car, C. Cavazzoni, D. Ceresoli, G. L. Chiarotti, M. Cococcioni, I. Dabo, A. Dal Corso, S. de Gironcoli, S. Fabris, G. Fratesi, R. Gebauer, U. Gerstmann, C. Gougoussis, A. Kokalj, M. Lazzeri, L. Martin-Samos, N. Marzari, F. Mauri, R. Mazzarello, S. Paolini, A. Pasquarello, L. Paulatto, C. Sbraccia, S. Scandolo, G. Sclauzero, A. P. Seitsonen, et al., *J. Phys. Condens. Matter Inst. Phys. J.* **2009**, *21*, 395502.
[34] J. P. Perdew, K. Burke, M. Ernzerhof, *Phys. Rev. Lett.* **1996**, *77*, 3865.
[35] S. Grimme, *J. Comput. Chem.* **2006**, *27*, 1787.
[36] H. J. Monkhorst, J. D. Pack, *Phys. Rev. B* **1976**, *13*, 5188.
[37] B. J. Kooi, J. Th. M. De Hosson, *J. Appl. Phys.* **2002**, *92*, 3584.
[38] A. Thumann, M. Schenk, J. Jonuscheit, T. Seeger, A. Leipertz, *Appl. Opt.* **1997**, *36*, 3500.

© 2020 The Authors. Physica Status Solidi (RRL) – Rapid Research Letters published by Wiley-VCH GmbH